Supporting information for "Magnetic resonance force microscopy with a one-dimensional resolution of 0.9 nanometers"

U. Grob,[†,§] M. D. Krass,[†,§] M. Héritier,[†] R. Pachlatko,[†] J. Rhensius,[†] J. Košata,[†] B. A. Moores,[†,‡] H. Takahashi,[†,¶] A. Eichler,[†] and C. L. Degen[*,†]

[†]*Department of Physics, ETH Zurich, Otto Stern Weg 1, 8093 Zurich, Switzerland.*

[‡]*Present address: JILA, National Institute of Standards and Technology and the University of Colorado, Boulder, Colorado 80309, USA and Department of Physics, University of Colorado, Boulder, Colorado 80309, USA.*

[¶]*Present address: JEOL RESONANCE Inc., Musashino, Akishima, Tokyo 196-8558, Japan.*

[§]*These authors contributed equally to this work.*

E-mail: degenc@ethz.ch

1 Nanomagnet Field Calibration

1.1 Fits to line scans

The magnetic field was approximated by separating its shape into short, cylindrical sections of constant magnetization. The field of a cylinder, homogeneously magnetized along its axis, can be expressed analytically. Adding the fields of all the sections provides the total field (see supporting information of Ref. 1). The diameter of each disc was calculated from a fit

to the mean diameter of an AFM scan, assuming an approximate rotational symmetry of the nanomagnet (see Sec. 1.3). The calibration of the magnetization was done experimentally, using the x scans described in the main article. From the known sample geometry, the expected MRFM signal was calculated and fitted to the experimental data (see Fig. S1). The simulation follows the supporting information of Ref. 1.

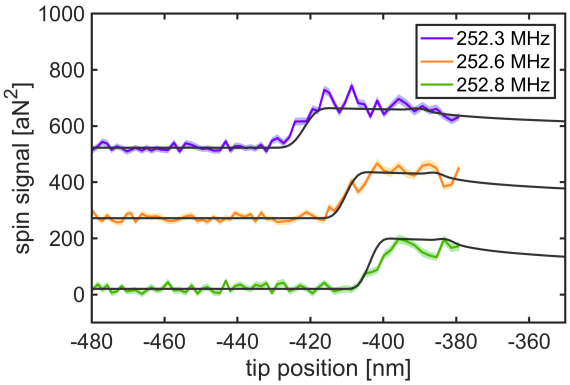

Figure S1: Simulated MRFM signals (black) fitted to three of the x scans presented in Fig. 4b of the main article. The magnetization of the nanomagnet was determined from this data. Here the tip position is referenced to the center of the nanomagnet. The curves are offset for better visibility.

We obtain a magnetization of the nanomagnet of $\mu_0 M_{\mathrm{magnet}} = 1.83\,\mathrm{T}$. The expected magnetic field gradients along x at different heights z above the nanomagnet's top surface are plotted in Fig. S2. We can expect a maximum magnetic field gradient of $6 \cdot 10^6\,\mathrm{T/m}$ between 10 and 20 nm above the nanomagnet.

1.2 Magnetic field gradient extracted directly from line scans

From the line scans for different resonant slices shown in Fig. 4b, we fit the signal onset position x_0. The scans were recorded $\sim 250\,\mathrm{nm}$ away from the edge of the nanomagnet where the gradient G_{x} varies slowly with distance. By plotting the onset position as a function of the slice frequency f_{rf} and fitting the slope S_{x_0} (see Fig. S3), we can estimate the

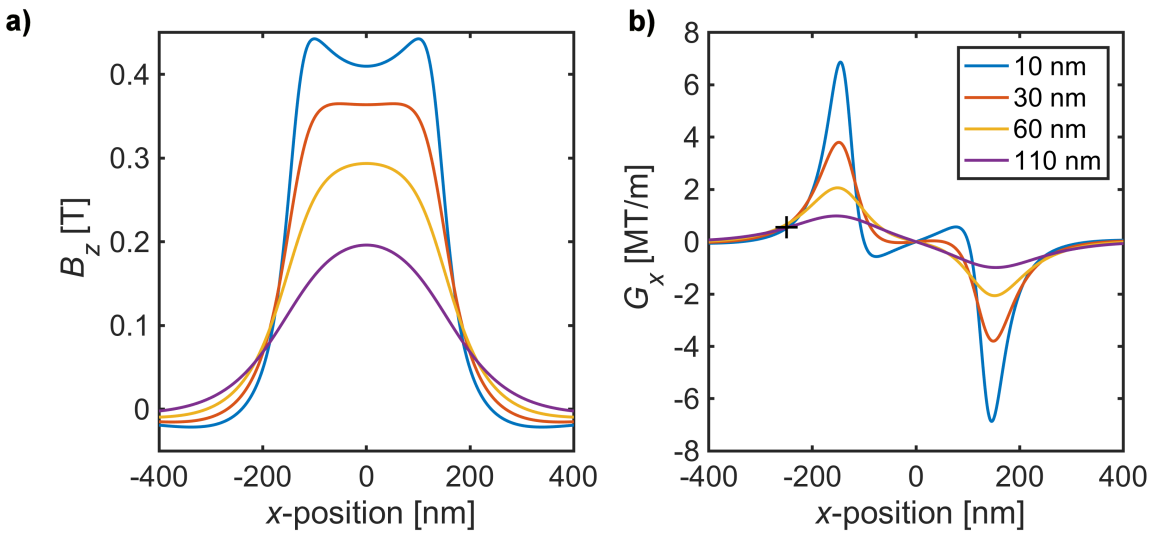

Figure S2: Magnetic field B_z (panel a) and magnetic field gradient G_x (panel b) for different heights above the nanomagnet. The curves were calculated from the experimentally calibrated tip model. The black cross denotes the experimentally determined magnetic field gradient in x-direction (see Fig. S3).

gradient at this position

$$G_x = \frac{1}{\gamma_n S_{x_0}} \,. \tag{S1}$$

For a slope of $S_{x_0} = 41.6 \cdot 10^{-15}\,\mathrm{m/Hz}$ we obtain a gradient of $G_x = 0.56 \cdot 10^6\,\mathrm{T/m}$.

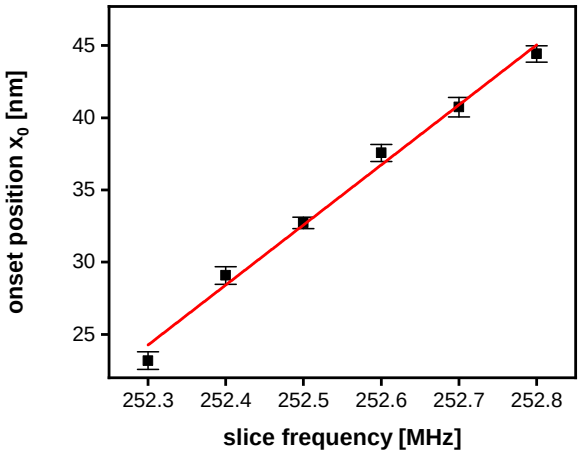

Figure S3: Linear fit of signal onset position x_0 as a function of slice frequency f_{rf}. From the slope we obtain a gradient $G_x = (41.6 \cdot 10^{-15}\,\mathrm{m/Hz} \cdot 42.58 \cdot 10^6\,\mathrm{T/m})^{-1} = 0.56 \cdot 10^6\,\mathrm{T/m}$.

1.3 Nanomagnet parameters

We infer the shape of the nanomagnet from an AFM scan. Assuming rotational symmetry, we calculate the mean radius as a function of height (gray curve in Fig. S4) and fit it in order to get a smooth shape (red curve in Fig. S4). The fit function is given by

$$h(r) = h_{\mathrm{mag}} \left[\frac{p}{1 + 10^{h_1 \cdot (r - b_1)}} + \frac{1 - p}{1 + 10^{h_2 \cdot (r - b_2)}} \right] , \tag{S2}$$

where the fit parameters $h_{\mathrm{mag}} = 213.9\,\mathrm{nm}$, $p = 0.84$, $h_1 = 2.559{\cdot}10^7\,\mathrm{m}^{-1}$, $h_2 = 6.957{\cdot}10^7\,\mathrm{m}^{-1}$, $b_1 = 191.7\,\mathrm{nm}$, and $b_2 = 230.2\,\mathrm{nm}$ were chosen to optimally resemble the magnet's top curvature.

We determine the magnetization of the nanomagnet to be $\mu_0 M_{\mathrm{magnet}} = 1.83\,\mathrm{T}$ with a magnetic bias field of $B_0 = 5.88\,\mathrm{T}$.

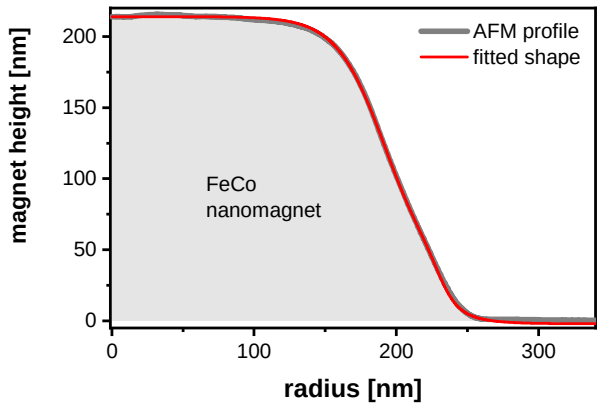

Figure S4: Cross section of the nanomagnet. The gray line is measured data, the red line is a fit that we use for our model.

2 Spin Simulations

2.1 Time evolution

We simulate the time evolution of a single spin operator $\hat{I}_z$ while applying an adiabatic full-passage pulse to estimate the slice function $\xi(\Delta f)$. To solve the *Liouville-von Neumann*

equation we use a time-discrete propagation of the spin density matrix $\rho(t)$. The time evolution by one time step Δt is given by

$$\rho(t+\Delta t) = \hat{U}(t+\Delta t)\rho(t)\hat{U}^{\dagger}(t+\Delta t) \ , \tag{S3}$$

where $\hat{U}(t)$ is the unitary operator

$$\hat{U}(t) = \exp\left(-i\ \hat{H}(t)\ \Delta t\right) \ . \tag{S4}$$

The Hamiltonian $\hat{H}(t)$ for an NMR pulse in the rotating frame can be written as

$$\hat{H}(t) = -2\pi\left[(f_{\mathrm{L}} - f_{\mathrm{rf,mod}}(t))\ \hat{S}_z + \gamma_{\mathrm{n}} B_{1,\mathrm{mod}}(t)\hat{S}_x\right] \tag{S5}$$

where $\hat{S}_x$ and $\hat{S}_z$ are the Pauli spin matrices, f_{L} is the spin's Larmor frequency, γ_{n} the nuclear gyromagnetic ratio, and where $f_{\mathrm{rf,mod}}(t)$ and $B_{1,\mathrm{mod}}(t)$ are the frequency and amplitude modulation of the NMR pulse, respectively. The expectation value of the spin along the external bias field B_0 is given by

$$\langle \hat{I}_z(t) \rangle = \mathrm{Tr}\left\{\rho(t)\hat{S}_z\right\} \ . \tag{S6}$$

All spin simulations shown in this paper were performed with a time step of $\Delta t = 0.5T_{\mathrm{c}}/314 \sim 1\,\mu\mathrm{s}$, where T_{c} is the cantilever period.

2.2 Pulse selection

In order to select the adiabatic pulse which performs best under our experimental conditions, we simulated the MRFM signal for a sample with a uniform spin density $\rho(\Delta f) = \rho$

$$\zeta = \delta_{\mathrm{slice}}\rho \int_{-f_{\mathrm{FM}}}^{f_{\mathrm{FM}}} a_1(f_{\Delta f})\mathcal{F}(f_{\Delta f})\ \mathrm{d}f_{\Delta f} \ , \tag{S7}$$

where δ_{slice} is the total slice width defined by the frequency range of $\mathcal{F}(\Delta f) \geq 0.1$, $a_1(\Delta f)$ is the Fourier coefficient, $\mathcal{F}(\Delta f)$ is the fidelity and $f_{\Delta f}$ varies the detuning of the spin from the carrier frequency f_{rf}. This definition of ζ is, in a first order approximation, proportional to the force signal F^2_{spin} and is used to compare the performance of different pulses. In Fig S5 we compare the MRFM signal as a function of the excitation bandwidth $2f_{\text{FM}}$ and the rf field amplitude B_1 for different types of adiabatic pulses.[2,3] For better comparison, the signal η is normalized for all simulations to the maximum value that occurred. The pulses indicated with (HS2^8) and (Gauss$-$5) show the best inversion efficiency for small inversion bandwidths $f_{\text{FM}} \leq 150\,\text{kHz}$. We chose the (HS2^8) pulse because it also shows very little dependence on B_1.

2.3 Robustness of HSn pulses

For three-dimensional magnetic resonance force microscopy (MRFM) imaging, the cantilever is scanned with respect to the magnetic tip. The scanning leads to variations of two crucial parameters of the adiabatic full-passage pulse, the maximum rf field amplitude B_1 and the pulse duration $T_{\text{p}} = (2f_{\text{c}})^{-1}$. The resonance frequency of the cantilever f_{c} strongly depends on the cantilever position relative to the magnet (see Sec. 3).

The class of HSn pulses is designed to provide a well-defined inversion profile as soon as a threshold field amplitude $B_{1,\text{threshold}}$ is exceeded.[4] We take advantage of this fact by setting B_1 well above $B_{1,\text{threshold}}$ to become insensitive to variations that occur within our typical MRFM scan range. Figure S6a compares the simulated fidelity $\mathcal{F}$ of an HSn pulse and a common trapezoidal pulse for small variations in B_1. Though simulated for a set of parameters resulting in the best inversion performance, the trapezoidal pulse slice varies strongly in shape while for the HSn pulse the difference is not visible. We also simulated the slice shape for a range of cantilever frequencies that are typically measured during a scan over the nanomagnet, as shown in Fig. S6b. For the HSn pulse, decreasing the pulse duration T_{p} from 390 µs to 210 µs only results in a reduction of the slice width of $\sim 20\,\%$. In

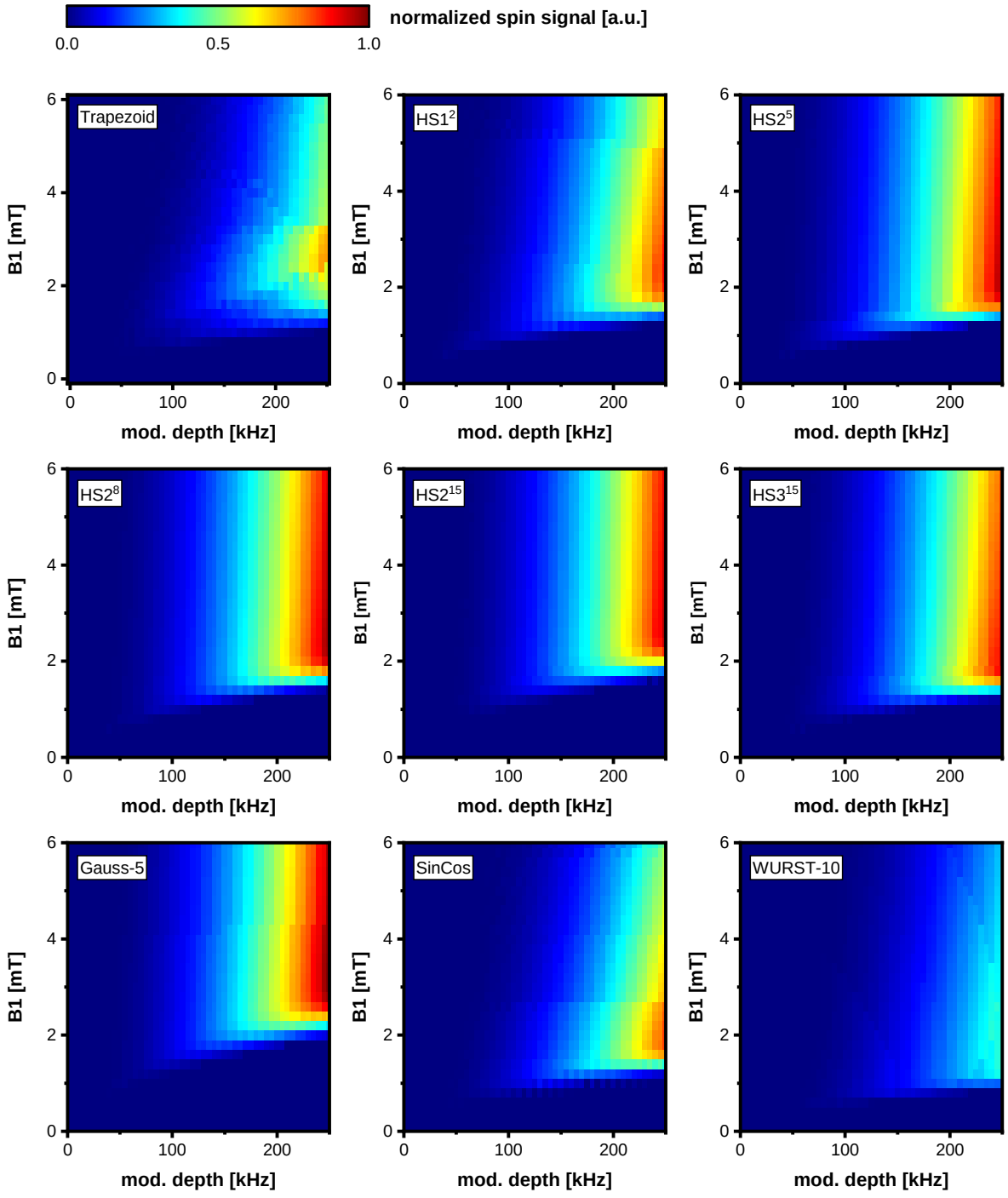

Figure S5: Adiabaticity simulations for several inversion pulses. All simulations are performed for ^{1}Hnuclei with $f_c = 3350\,\mathrm{Hz}$ and $N = 140$ Inversions. The signal η is normalized for all simulations by the same value.

contrast, at the highest cantilever frequency the trapezoid pulse does not achieve a fidelity $\mathcal{F} = 1$ for any spin within the excitation bandwidth. Both sets of simulations confirm that the HSn pulse is well suited for high resolution MRFM experiments.

2.4 Difference in settings between Fig. 2d and 2e

In Fig. 2d, the spin inversion fidelity $\mathcal{F}$ as a function of the nuclear spin detuning Δf was calculated for a cantilever frequency $f_c = 3350\,\mathrm{Hz}$, a modulation depth $f_{\mathrm{FM}} = 150\,\mathrm{kHz}$, and an in-plane field amplitude $B_1 = 5.3\,\mathrm{mT}$. The transformation from detuning to spatial distance $\Delta x = \Delta f \cdot \gamma^{-1} \cdot G_x^{-1}$ (top scale in Fig. 2d) takes into account a gradient of $G_x = 2 \cdot 10^6\,\mathrm{T/m}$. For this set of parameters the adiabatic condition for the inversion pulses is sufficiently fulfilled,[4] hence we obtain a well-defined and box-like inversion profile.

To record the data presented in Fig. 2e the cantilever was positioned centered over the magnet's edge at a distance of 25 nm and we swept the modulation depth f_{FM}. Due to the cantilever-magnet interaction the resonance frequency shifted to $f_c = 4820\,\mathrm{Hz}$, resulting in a 40 % faster inversion rate. We detected a signal with SNR > 1 with modulation depths as small as $f_{\mathrm{FM}} = 75\,\mathrm{kHz}$. A simulation of the inversion profile for the given parameters confirmed that the adiabatic condition is no longer fulfilled. The fidelity does not reach the maximum value of $\mathcal{F}_{\mathrm{max}} = 1$ for any spin within the resonant slice, resulting in a different shape than shown in Fig. 2d. Therefore, the minimal total slice width in this experiment with $G_x = 2.3 \cdot 10^6\,\mathrm{T/m}$ was $\delta_{\mathrm{slice,min}} = 0.7\,\mathrm{nm}$, not $\delta_{\mathrm{slice,linear}} = 1.2\,\mathrm{nm}$ as a linear scaling with G_x and f_{FM} would suggest. Note that we define $\delta_{\mathrm{slice,min}} = 0.7\,\mathrm{nm}$ as the spatial range for $\mathcal{F} \geq 0.1$. The effective width defined by, e.g., $\mathcal{F} \geq 0.5$, would be even smaller.

2.5 Calibration of B1

The fidelity of adiabatic full-passage pulses depends on the maximum rf field amplitude B_1 at the position of the spin. In the experiment, B_1 is controlled by the voltage amplitude of the arbitrary waveform generator U_{AWG} driving the rf stripline antenna.

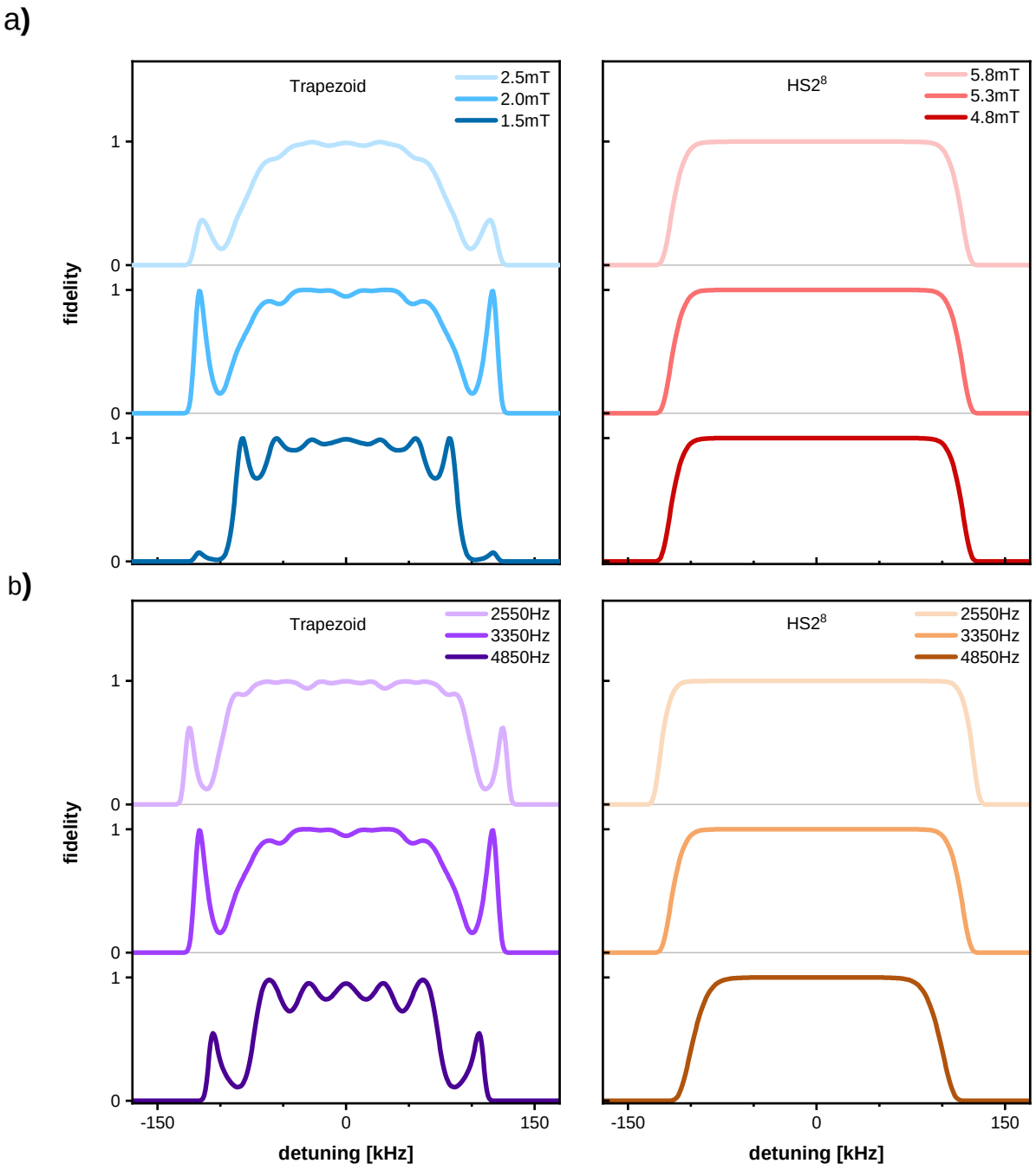

Figure S6: Simulated inversion profiles. Individual curves are offset for better comparison. (a) Trapezoidal and HS2[8] pulse profile as a function of B_1 for $f_c = 3350\,\mathrm{Hz}$. (b) Pulse profile as a function of pulse duration $T_p = 1/2f_c$ for $B_1(\mathrm{Trap}) = 2.0\,\mathrm{mT}$ and $B_1(\mathrm{HS2^8}) = 5.3\,\mathrm{mT}$.

We performed a adiabaticity measurement by recording the MRFM signal as a function of U_{AWG} and f_{FM} and compared it to the simulation shown in Fig S5. The signal onset at $B_{1,\mathrm{onset}} \sim 1.5\,\mathrm{mT}$ provides a distinct feature which allows an easy and reliable alignment of both signals. Additionally, we measured the transmission parameters of the rf circuit and calculated the expected magnetic field for the applied voltage amplitude U_{AWG}. Both values are in good agreement, resulting in a $B_1 = 5.3\,\mathrm{mT}$ for the data shown in Fig 2e.

3 Cantilever Sensitivity Calibration

In MRFM, as in many other AFM-based techniques, the quantity of interest is the force acting on the transducer. Therefore, a careful calibration of the spring constant of the cantilever k_{c} is essential for any quantitative measurement.

We calibrate the spring constant by a fit of the thermally driven power spectral density spectrum S_{xx} at room temperature (see Fig. S7). The expected shape of the spectrum is given by[5]

$$S_{xx}(f) = \frac{2k_{\mathrm{B}}T f_{\mathrm{c}}}{\pi m_{\mathrm{c}} Q_{\mathrm{c}}} \cdot \frac{1}{\left(f_{\mathrm{c}}^2 - f^2\right)^2 + Q_{\mathrm{c}}^{-2}\left(f_{\mathrm{c}} f\right)^2} \,, \tag{S8}$$

where k_{B} is the Boltzmann constant, T the absolute temperature of the cantilever eigenmode, f_{c} the free resonance frequency, Q_{c} the quality factor and m_{c} the dynamic mass of the cantilever. From independent ring-down experiments we determine $Q_{\mathrm{c}} = \pi f_{\mathrm{c}} \tau$, where τ is the exponential decay time of the amplitude. The eigenmode temperature T is measured with a temperature sensor integrated in the MRFM probe head. For good thermalization and an accurate temperature reading, the spectrum is recorded at room temperature. This is a standard procedure often used for calibrating AFM cantilevers.[5,6]

The forces that act on the cantilever during a MRFM measurement are generated at the tip position where the sample is located. The cantilever motion, however, is detected at a small mirror paddle, which is offset from the tip apex and leads to a reduced sensor signal.

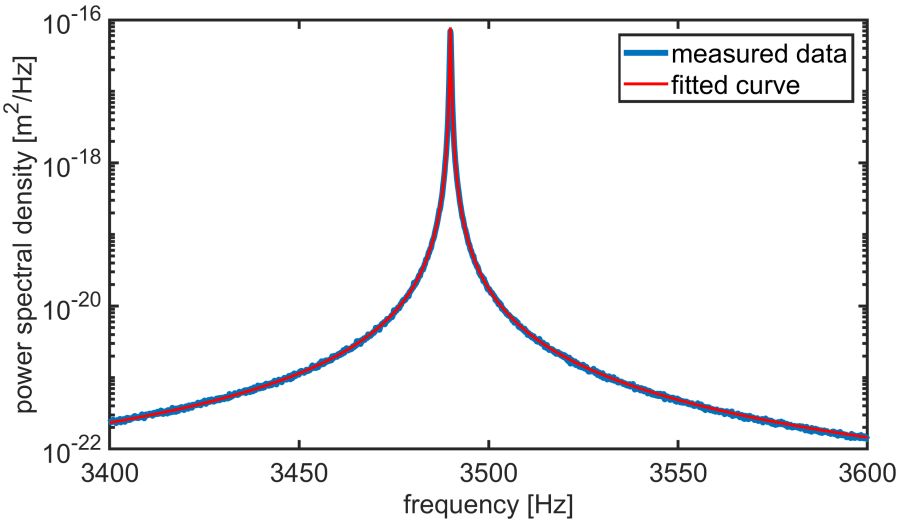

Figure S7: Power spectral density of the cantilever used for this work. The dynamic mass m_c has been calibrated by the fitted curve. The parameters for the free cantilever are $f_c = 3489.9\,\mathrm{Hz}$, $m_c = 1.70 \cdot 10^{-13}\,\mathrm{kg}$, and $k_c = 81.7\,\mu\mathrm{N/m}$ at room temperature; at cryogenic temperatures the free cantilever resonance frequency shifts to approximately 3522 Hz.

We performed a finite element analysis (Siemens NX Nastran) to obtain a leverage factor a_c that compensates for the reduction of the signal read-out. The model incorporates the exact geometry of the cantilever including the glued-on nanorod which was determined from a high-resolution optical microscope image. The amplitude distribution of the first cantilever eigenmode is depicted in Fig. S8.

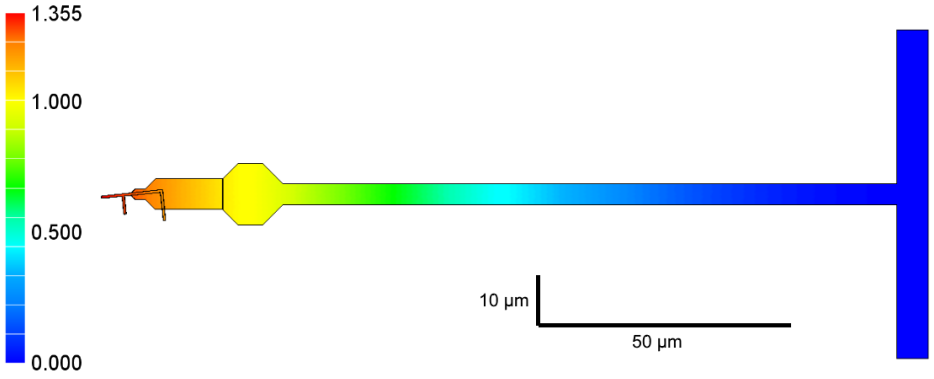

Figure S8: Amplitude distribution of the first cantilever eigenmode including the glued on nanowire. It has been normalized to the amplitude of the deflection read out location at the small mirror paddle, resulting in a leverage factor $a_c = 1.355$.

Compared to other AFM methods ($k_{\mathrm{AFM}} \sim 0.1 - 40\,\mathrm{N/m}$), we use very soft cantilevers

($k_c \sim 80\,\mu N/m$) which are strongly influenced by the surrounding energy landscape. In proximity to the nanomagnet, detected resonance frequencies f_c^* can range from 1 kHz to 10 kHz. This frequency shift is associated with a change of the effective spring constant k_c^*. Detailed analysis of the effect of an external interaction at the very tip of the cantilever showed that the relation

$$k_c^* = m_c \cdot (2\pi f_c^*)^2 , \tag{S9}$$

is valid up to about twice the free cantilever resonance frequency. Above this range a node starts to develop at the tip of the cantilever due to the external potential which alters the eigenmode structure of the cantilever to where it can no longer be modeled as the original simple harmonic oscillator with a small correction. Since the dynamic mass m_c, obtained from the fit in Fig. S7, does not change under normal experimental conditions, we can use the cantilever frequency f_c^* at each scan position to determine the effective spring constant k_c^*.

4 Nanorod Fabrication and Attachment

We use batch-fabricated silicon nanorods with a cross-section of $\sim 300\,nm \times 500\,nm$ as sample attachment platform. They are prepared independently from the cantilever and attached after their specific treatment is complete. They feature a lower surface roughness and a smaller cross-section than the cantilever tip, which reduces the non-contact friction between the cantilever and the nanomagnet and results in a better sensitivity.

The nanorods are made from silicon on insulator (SOI) wafer chips (4“ diameter, 4 µm device layer thickness, 6 µm oxide layer thickness) using the following recipe:

- Dice chips into 2.5 cm × 2.5 cm pieces
- Thin device layer uniformly down to ∼ 300 nm with a TMAH solution (25 % tetram-

ethylammonium hydroxide in water)

- Write nanorod pattern with electron-beam lithography
- Etch straight sidewalls with inductively coupled plasma (ICP)
- Under-etch nanorods $\sim 3\,\mu m$ in buffered hydrofluoric acid (BHF, 7 % in water)
- Evaporate gold on nanorods (for screening trapped charges and as an adhesion layer for biological samples)

The scanning electron micrograph in Fig. S9 shows a finished chip with nanorods attached via easily breakable silicon beams. A nanorod is glued to the cantilever tip under a microscope with the use of manual micro-manipulators. We use a epoxy-based adhesive (Alradite, 5 min) which cures even for a very small volume at room temperature within reasonable time ($\sim 20 - 30\,min$). Finally, the nanorod is broken loose from the chip by wiggling the cantilever.

This modular approach has the advantage that the sample preparation is carried out separately from the mechanical transducer. Biological samples, like virus particles or cell membranes, are usually deposited from a nutrient solution which could leave residuals behind that degrade the mechanical properties of the cantilever.

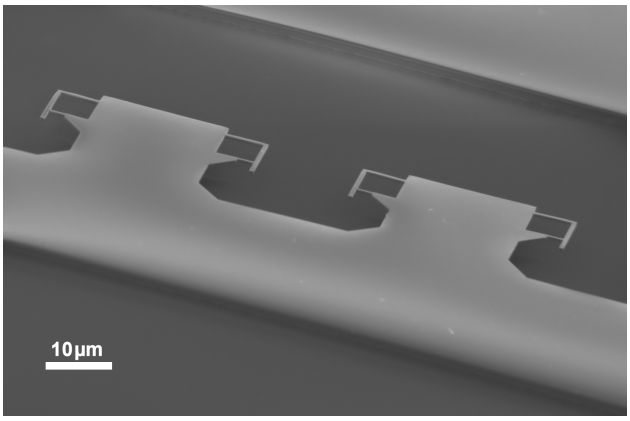

Figure S9: Scanning electron microscopy image of nanorods, still attached to their breakaway bridges, ready to be glued to a cantilever tip and separated from their chip.

5 Calibration of Scan Position

In MRFM scanning experiments the cantilever is moved relative to a magnetic tip by a piezoelectric actuator. To determine the lateral resolution of our apparatus, the piezoelectric constant S_{scan} is of great importance. Further, for the very compliant transducer we use ($\sim 10^{-4}\,\mathrm{N/m}$), the cantilever-magnet interaction leads to significant static deflections of the tip respectively the sample which have to be taken into account.

The scanner is calibrated in-situ under experimental conditions by performing an AFM-type measurement of the stripline-nanomagnet chip with the MRFM cantilever. By comparing the image to a reference scan taken at room temperature with a conventional AFM, we obtain S_{scan}. Static deflections of the cantilever and the blunt shape of the nanorod are considered in this analysis.

The cantilever motion is measured via an optical interferometer which is sensitive to both the static cantilever deflection and the dynamic oscillations. During a scan, the interferometer is kept at its most sensitive operation point by tuning the laser wavelength via a PID controller. Therefore, the cantilever tip position x_{tip} is given by

$$x_{\mathrm{tip}} = S_{\mathrm{scan}}\, U_{\mathrm{scan}} + S_{\mathrm{PID}}\, \Delta U_{\mathrm{PID}} + S_{\mathrm{DC}}\, U_{\mathrm{PID,error}}\ , \tag{S10}$$

where U_{scan} is the voltage applied to the piezo actuator, $x_{\mathrm{scan}} = S_{\mathrm{scan}}\, U_{\mathrm{scan}}$ is the nominal scanner position, S_{PID} is the tuning sensitivity of the PID controller, ΔU_{PID} is the PID output voltage relative to a reference point with no cantilever-magnet interaction, S_{DC} is the sensitivity of the interferometer to static deflections, and $U_{\mathrm{PID,error}}$ is the residual error of the PID controller. Due to the slow scanning speeds in MRFM scans of less than 1 nm/min, the last term in Eq. S10 is negligible.

6 Nonlinear Fit of Signal Onset

6.1 Onset position uncertainty

We note that there are similarities between measuring spin density in a sample with a linearly scanned resonant slice (cf. Fig. 4b) and estimating the position of a grating edge under an optical microscope with the help of a scanned slit.[7] In both cases, the signal corresponds to the convolution of the profile of a scanning probe (slice/slit) and the sample geometry. The precision with which the position of an edge can be determined is limited by the noise superimposed on the rising signal. For optical microscopy, the standard error of the corresponding position estimation can be rigorously derived for a linear fit.[7] In close analogy, we used a nonlinear fit curve (hyperbolic tangent) for our data in Fig. 4b and defined the uncertainty of the sample edge position from the 68.3 %-confidence interval of the fit. The resulting number is $\sigma_{x_0} = 0.6\,\mathrm{nm} \pm 0.1\,\mathrm{nm}$, as stated in the main text.

In a second step, we can define a limit for measuring the same feature (i.e., the same sample edge) with various 'slits'. This is precisely what we have done in Fig. 4b by using different slices to obtain slightly shifted signals. The smallest spatial shift between two traces we can discern in this way is derived from basic error propagation. We find that the corresponding uncertainty is $\sigma_{\Delta x} = \sqrt{\sigma_{x_0,1}^2 + \sigma_{x_0,2}^2} = 0.9\,\mathrm{nm} \pm 0.2\,\mathrm{nm}$, exactly the same as our SNR-limited resolution.

6.2 Signal rise distance

From the fits to individual scans shown in Fig. 4b, we obtain a typical signal rise width of $w \sim 10\,\mathrm{nm}$. This width is mainly determined by the convolution of the sample with the residual curvature of the tangential imaging slice and is not indicative of the spatial resolution. In the case of comparable sizes of sample width and slice diameter ($\sim 300 - 500\,\mathrm{nm}$), the rise distance is mainly determined by the slice width. This is confirmed by the slice profile shown in Fig. 2d which translates for $G_x = 0.56 \cdot 10^6\,\mathrm{T/m}$ to a total width of $w_{\mathrm{slice}} = 10.7\,\mathrm{nm}$.

References

(1) Degen, C. L.; Poggio, M.; Mamin, H. J.; Rettner, C. T.; Rugar, D. *Proceedings of the National Academy of Sciences of the United States of America* **2009**, *106*, 1313.

(2) Tannus, A.; Garwood, M. *Journal of Magnetic Resonance. Series A* **1996**, *120*, 133–137.

(3) Bendall, M. R.; Pegg, D. T. *Journal of Magnetic Resonance* **1986**, *67*, 376 – 381.

(4) Tannús, A.; Garwood, M. *NMR in biomedicine* **1997**, *10*, 423–34.

(5) King, W. T. Thermal cantilever calibration. 2009; https://www.physics.drexel.edu/~wking/rsrch/papers/cantilever_calib/, Accessed date: 2019-07-28.

(6) Cook, S. M.; Lang, K. M.; Chynoweth, K. M.; Wigton, M.; Simmonds, R. W.; Schäffer, T. E. *Nanotechnology* **2006**, *17*, 2135–2145.

(7) Köning, R.; Karovič, K.; Wimmer, G.; Witkovský, V. *Metrologia* **2012**, *49*, 169–179.